Supplementary Information

Unveiling the Synergistic Piezo-Phototronic Dynamics in Indium Selenide incorporated Poly(vinylidene fluoride) based Nanocomposites for Next-Generation Energy Harvesting

*Ananya Aishwarya[1], Urosa Latief[2], Abhishek Naskar[1], Jitendra Pratap Singh[2], Arup R. Bhattacharyya[1]**

[1]Department of Metallurgical Engineering and Materials Science, Indian Institute of Technology Bombay, Powai, Mumbai 400076, India

[2]Department of Physics, Indian Institute of Technology Delhi, New Delhi 110016, India

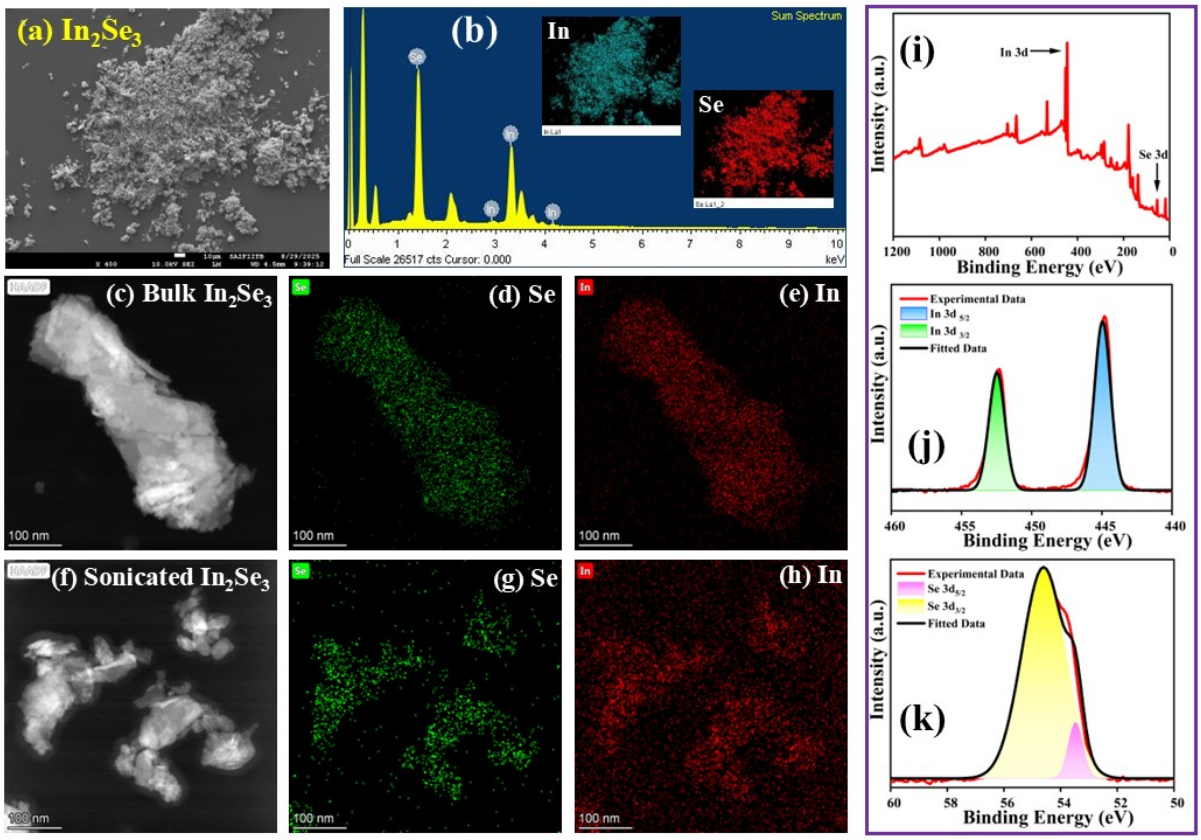

Figure S1 (a) SEM image of sonicated In_2Se_3 flakes, (b) EDS mapping and spectra obtained from SEM of In_2Se_3 flake, (c)-(h) EDS mapping of (c)-(e) bulk In_2Se_3, (f)-(h) sonicated In_2Se_3 obtained from TEM image, (i)-(k) XPS spectra of unsonicated bulk In_2Se_3.

Fig. S1 presents the morphological, compositional, and surface chemical characterization of bulk and sonicated In_2Se_3. The SEM image presented in Fig. 1(a) shows that the sonicated In_2Se_3 flakes possess an agglomerated and layered morphology, confirming successful exfoliation from bulk aggregates into few-layered nanosheets. The corresponding EDS spectrum depicted in Fig. S1(b) verifies the elemental composition with distinct peaks for indium (In) and selenium (Se), and the elemental maps further confirm the homogeneous spatial distribution of both elements across the sample. The TEM-EDS mappings shown in Fig. 1(c)-(h) reveal that the bulk In_2Se_3 (shown in Fig. S1(c)-(e)) exhibits a dense and compact morphology, whereas the sonicated In_2Se_3 (show in Fig. S1(f)-(h)) shows reduced thickness and lateral dimensions, indicating effective delamination induced by ultrasonication. The uniform dispersion of In and Se signals in the sonicated flakes supports compositional stability after exfoliation. The XPS spectra shown in Fig. S1(i)-(k) provide further evidence of the chemical states of In and Se in bulk In_2Se_3. The survey spectrum presented in Fig. S1(i) displays characteristic peaks corresponding to In 3d and Se 3d orbitals, confirming the purity of the material. The high-resolution spectra depicted in Fig. S1(j, k) show binding energies at ~ 444.6

eV and ~ 452.1 eV for In $3d_{5/2}$ and In $3d_{3/2}$, respectively, and at ~54.6 eV for Se $3d_{5/2}$, consistent with the presence of In^{3+} and Se^{2-} oxidation states typical of crystalline In_2Se_3 [1].

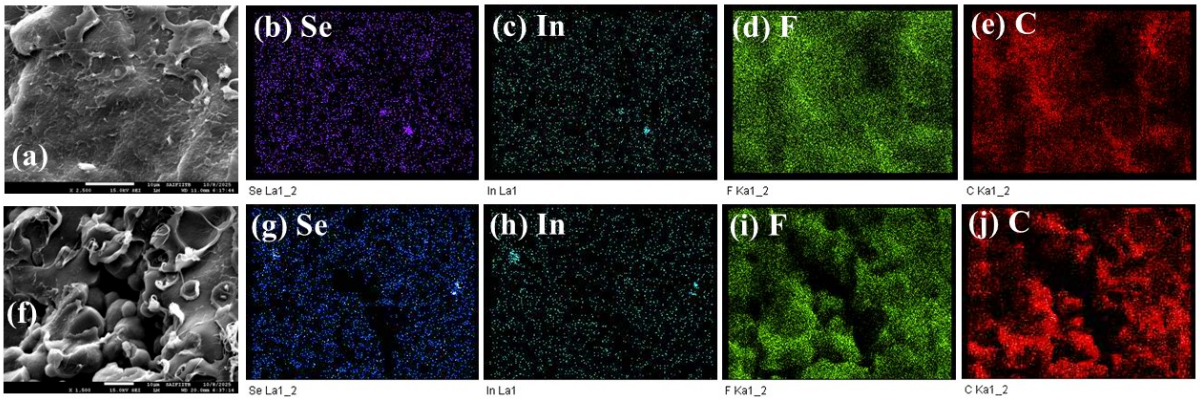

Figure S2 (a)-(i) SEM image of cryo-fractured PVIS_2 nanocomposite film and corresponding EDS mapping depicting various elemental distribution of PVIS_2 nanocomposite.

Fig. S2 shows scanning electron microscopic (SEM) images of a cryo-fractured PVIS_2 nanocomposite film and corresponding energy-dispersive X-ray spectroscopy (EDS) mapping of the elemental distribution in the nanocomposite. Fig. S2(b)-(e) and (g)-(j) provide elemental maps for selenium (Se), indium (In), fluorine (F), and carbon (C). In particular, the mapping images (b) and (g) highlight the distribution of Se, showing it in purple, while (c) and (h) map In in turquoise, (d) and (i) show the fluorine distribution in green, and (e) and (j) represent the carbon distribution in red. These images reveal the spatial arrangement and homogeneity of the elements within the PVIS_2 nanocomposite film. The SEM and EDS data together offer valuable insight into the structural and elemental composition of the material, which is crucial for understanding its properties and potential applications.

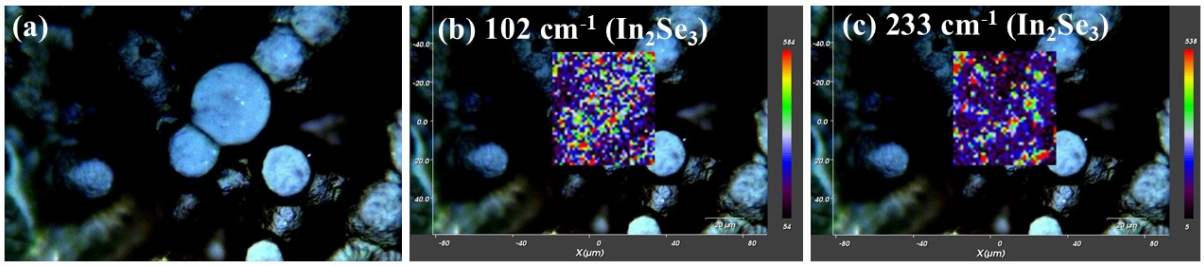

Figure S3 Raman mapping of PVIS_2 nanocomposite for 102 cm^{-1} and 233 cm^{-1} peaks for In_2Se_3.

Fig. 3 presents Raman mapping of the PVIS_2 nanocomposite, specifically focusing on the 102 cm^{-1} and 233 cm^{-1} peaks that correspond to the In_2Se_3 phase within the composite material. Fig. S3(a) shows the spherulitic structures of the PVIS_2 nanocomposite, where the different components of the film are visible. Fig. S3(b) displays the Raman map of the 102 cm^{-1} peak, associated with In_2Se_3, where the distribution of the phase is depicted in a colourful spectrum

indicating intensity variation. Similarly, Fig. S3(c) shows the Raman map for the 233 cm^{-1} peak, further confirming the presence and distribution of In_2Se_3 within the nanocomposite. The coloured maps help visualize how In_2Se_3 is distributed across the PVIS_2 nanocomposite, providing insight into the structural composition of the nanocomposite at the molecular level. These maps are useful for understanding the phase distribution and homogeneity of In_2Se_3 within the PVDF matrix.

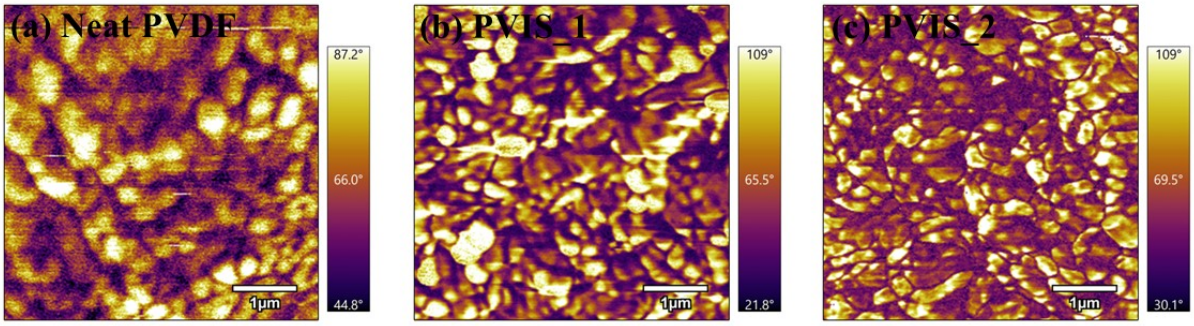

Figure S4 Variation of phase images obtained from PFM analysis for (a) neat PVDF, (b) PVIS_1 and (c) PVIS_2 nanocomposite.

Fig. S4 shows phase images obtained from piezoresponse force microscopy (PFM) analysis for neat PVDF (Fig. S4(a)), (b) PVIS_1 (Fig. S4(b) and (c) PVIS_2 nanocomposite (Fig. S4(c)). The phase images reveal the distribution of the polarization phase across the surface of each sample. Fig. S4(a) represents the neat PVDF, where the phase contrast reveals a relatively uniform pattern with a phase variation between 44.8° and 87.2°, suggesting the presence of localized polar domains. In Fig. S4(b), depicting the phase image of PVIS_1 nanocomposite, the phase contrast becomes more pronounced, with a wider variation in phase (21.8° to 65.5°), indicating a more heterogeneous domain structure. In Fig. S4(c), for the PVIS_2 nanocomposite, the phase distribution is further enhanced, with values ranging from 30.1° to 109°, suggesting a more complex and organized polarization behaviour, likely influenced by the inclusion of the In_2Se_3 nanoparticles. These PFM images provide insight into the ferroelectric or piezoelectric properties of the different materials and their respective domain structures, which are crucial for their potential applications in electronic and energy storage devices [2].

Table S1 Roughness parameter obtained for neat PVDF, PVIS_1 and PVIS_2 nanocomposite films.

Sample	Height (nm)	Depth (nm)	Roughness (nm)
Neat PVDF	110.3	131.1	121.1

PVIS_1	145.6	152.7	149.2
PVIS_2	210.5	175.3	193.7

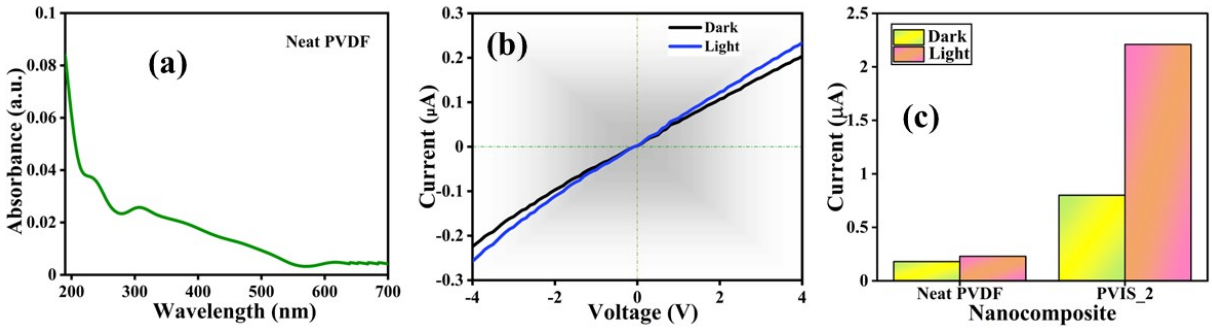

Figure S5 UV-vis response of neat PVDF, (b) current-voltage measurements under dark and illuminated conditions for neat PVDF film and (c) comparison of photo-current obtained in on and off mode for neat PVDF and PVIS_2 nanocomposite film.

Fig. S5 presents key experimental data on the UV-vis absorption and photoelectric response of neat PVDF and PVIS_2 nanocomposite. Fig. S5(a) shows the UV-vis absorption spectrum of neat PVDF, with the x-axis representing wavelength (200 to 700 nm) and the y-axis representing absorbance. The plot reveals that neat PVDF absorbs strongly in the UV region, below ~ 300 nm, but has minimal absorbance in the visible range (above 400 nm), indicating its limited light absorption in this region. This serves as a baseline for comparison with the PVIS_2 nanocomposite.

Fig. S5(b) illustrates the current-voltage (I-V) characteristics of neat PVDF under both dark (black curve) and illuminated (blue curve) conditions. Under dark conditions as well as when exposed to light, the current response of the neat PVDF film is near linear with minimal variation, suggesting negligible photoelectric activity. Fig. S5(c) compares the photo-current generated in neat PVDF and PVIS_2 nanocomposite films under both dark and illuminated conditions. Fig. S5(c) represents the current generated by neat PVDF which shows that a small photo-current under both dark and light conditions is obtained. In contrast, the PVIS_2 nanocomposite film produces a much higher photo-current, indicating that the addition of the nanocomposite enhances the material's ability to generate photo-induced current. This suggests that the PVIS_2 nanocomposite improves the photoelectric properties of the PVDF film, making it more suitable for applications requiring light-sensitive electrical behaviour [3].

Overall, the Fig. S5 demonstrates the UV-vis absorption and photoelectric properties of both neat PVDF and the PVIS_2 nanocomposite. The data highlights the limited light absorption of

neat PVDF and its photoelectric response under illumination, while showing a significant improvement in the photo-current when the PVIS_2 nanocomposite is incorporated. This enhancement suggests that the nanocomposite can potentially be used in applications that require improved light harvesting and photo-induced electrical activity [4].

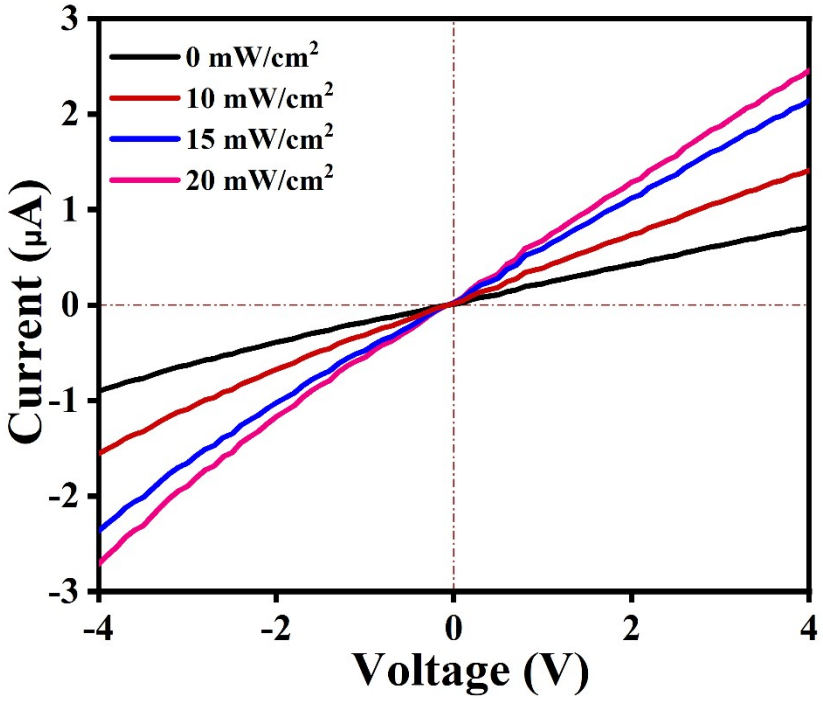

Figure S6 Comparison of photo response current of PVIS_2 at different illumination intensities.

The device exhibits a very low dark current under applied bias, and with increasing light intensity, the photocurrent increases systematically, reaching ~ 2.21 μA at 20 mW/cm^2. The nearly linear and symmetric I-V behaviour indicates good electrical contact between the PVIS_2 nanocomposite and the Au/Cr electrodes, minimizing contact-induced artifacts. Importantly, the measurable and intensity-dependent photocurrent under illumination alone confirms the intrinsic semiconducting photoactivity of the α-In_2Se_3 incorporated system.

By establishing (i) the independent photoresponse under illumination-only conditions and (ii) the enhanced output under simultaneous mechanical and optical excitation (discussed in the main manuscript), the revised analysis more clearly supports the existence of strain-modulated photo-carrier transport consistent with piezo-phototronic coupling. While phase-resolved dynamic measurements could provide further quantitative decoupling and represent an interesting direction for future study, the present additional controls strengthen the mechanistic interpretation within the scope of this work.

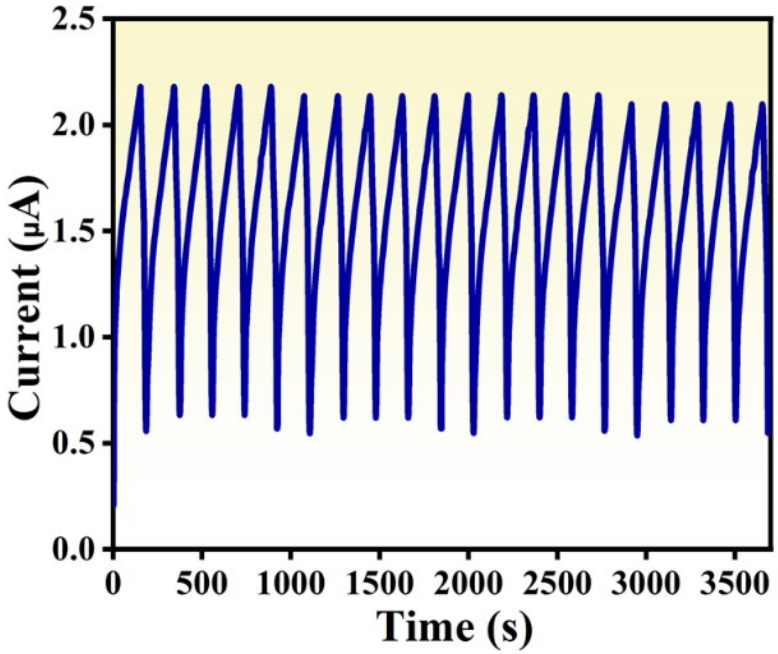

Figure S7 Photocurrent characteristics of the device over 20 continuous cycles

Table S2 Comparison of electroactive phase content with various piezoelectric parameters for neat PVDF, PVIS_1 and PVIS_2 nanocomposite films.

Sample	Polar phase (%)	d_{33} value (pm/V)	Output voltage (V)	Power density ($\mu W/cm^2$)	Current Density ($\mu A/cm^2$)
Neat PVDF	35.4	20.2	14.5	5.9	1.3
PVIS_1	69.2	42.8	53.4	42.8	1.52
PVIS_2	91	53.4	70.5	46.6	1.64

References

1 W. Ding, J. Zhu, Z. Wang, Y. Gao, D. Xiao, Y. Gu, Z. Zhang and W. Zhu, *Nat Commun*, 2017, **8**, 1–8.

2 A. Aishwarya, A. Naskar, T. Dasgupta and A. R. Bhattacharyya, *J Alloys Compd*, 2025, **1036**, 182155.

3 A. Ajayakumar, C. Muthu, A. V. Dev, J. K. Pious and C. Vijayakumar, *Chem Asian J*, 2022, **17**, e202101075.

4 K. Maity, U. Pal, H. K. Mishra, P. Maji, P. Sadhukhan, Z. Mallick, S. Das, B. Mondal and D. Mandal, *Nano Energy*, 2022, **92**, 106743.